

Contents lists available at ScienceDirect

# Journal of the European Ceramic Society

journal homepage: www.elsevier.com/locate/jeurceramsoc





# Localization of embrittlement in CMAS-infiltrated thermal barrier coatings via laser shock experiments

Capucine Billard <sup>a,b</sup>, Christoph Mikulla <sup>c</sup>, Vincent Guipont <sup>a</sup>, Ravisankar Naraparaju <sup>c</sup>, Uwe Schulz <sup>c</sup>, Vincent Maurel <sup>a,\*</sup>

- <sup>a</sup> MINES Paris, PSL University, MAT Centre des Matériaux, CNRS UMR 7633, 21 All. des Marronniers, Versailles 78000, France
- <sup>b</sup> Safran Aircraft Engines Villaroche, Rond-Point René Ravaud, Moissy-Cramayel 77550, France
- <sup>c</sup> German Aerospace Center (DLR), Institute of Materials Research, Linder Hoehe, Cologne D-51147, Germany

#### ARTICLE INFO

Keywords: TBC CMAS LASAT Embrittlement Infrared thermography

#### ABSTRACT

As the operation temperature of aero-engine increases, the threat of molten deposits, usually caused by volcanic ash or sand ingestion has a major concern to the durability of these systems. In thermal barrier coatings, the ceramic topcoat (TC) layer made of partially stabilized zirconia is highly sensitive to such corrosive attack by means of infiltration, causing their premature failure. Infiltration causes either a decrease in toughness and adhesion or an increase in stiffness of the TC layer. As a local method to assess the interface strength of TBCs, the Laser Shock Adhesion Test (LASAT) is investigated for the first time to a columnar ceramic coating with and without infiltration by a CMAS deposit. LASAT clearly shows the location of the minimum toughness zone within TC layer, which is associated with the zone of infiltration, the infiltration depth limit or the TGO/topcoat interface. This is key to assessing the mechanical weakening from such corrosive attack.

# 1. Introduction

The infiltration of molten deposits in modern aero engines has been identified as a major concern regarding the drastic effects on components when exposed to natural volcanic ash (VA), sand or synthetic CaO-MgO-Al<sub>2</sub>O<sub>3</sub>-SiO<sub>2</sub> (CMAS). Thermal Barrier Coatings (TBC) are dramatically sensitive to CMAS attack because they are used to protect the hottest parts of the turbine made of superalloys (combustion chambers, high-pressure turbine blades or vanes) [1–3]. TBCs are multilayered systems consisting of a ceramic topcoat (TC), which reduces the temperature reaching the Ni-based substrate and usually consists of YSZ (Yttria Stabilized Ziconia), a bond-coat (BC) layer, that acts as a reservoir of Al to form a thermally grown oxide (TGO) layer between TC and BC layers. During operation, the surface temperature regularly exceeds the melting point of the CMAS/VA, enabling the infiltration of the molten deposit into the porosity of the TBC.

There are two main aspects of CMAS infiltration to consider. One is a global corrosive attack that could modify the chemistry of the topcoat material down to the TGO layer by means of deeper infiltrations [3,4]. The chemical reaction causes the phase transformation of TC from tough tetragonal prime phase t' into monoclinic phase m or cubic phase c [5].

For a columnar TC structure (processed by EB-PVD or SPS) optimized to improve the strain tolerance of the TC layer, CMAS infiltration yields to a continuous dense layer of increased stiffness, which is thought to promote easier spallation of the TC, or at least the spallation of the infiltrated part of the TC [6]. However, the potential role of either increased stiffness or increased embrittlement due to decreased mechanical toughness in premature failure is still an open question. The nature of CMAS (composition and particle size distribution) and condition of exposure (maximum temperature, temperature gradient and duration of exposure) yielding very complex picture of CMAS infiltration and damaging effects [7–10]. Research on CMAS mitigation strategies currently focuses on adaptation of TBC material e.g., reactive rare earth zirconates like yttria-rich zirconia or gadolinium zirconate [11] or microstructural optimization [4,12].

The LAser Shock Adhesion Test (LASAT) is a local method to evaluate the adhesion strength of ceramic top coats. The method is based on the use of a nanosecond LASER to promote ablation by laser-matter interaction, e.g., on the metallic side of a typical TBC system. The Laser initially induces a compressive front shock wave, followed by its release wave which, after reflection at the free surface of the material, becomes mostly a released shock wave leading to tensile stress when and where

E-mail address: vincent.maurel@mines-paristech.fr (V. Maurel).

<sup>\*</sup> Corresponding author.

both release waves cross over. Since this tensile region resulted from the temporal and spatial distribution of the shock wave, it promotes cracking of the weak points of a layered system. For TBC exposed to lab air oxidation (without CMAS), cracking is mostly observed in the vicinity of the TGO layer. The associated mechanical toughness can be assessed by calibration for further comparison of aging conditions on the same coated sample [13].

One of the main features of LASAT is that the dynamic loading associated with the shock wave is homogeneous over a very large distance associated with the size of the irradiated area itself and orthogonal to the interface. To simplify the way LASAT could initiate a crack in a TBC system, it could be associated with a uniform stress in tension orthogonal to the shock wave propagation. Edge propagation effects have been also demonstrated to reach crack diameter higher than the shock diameter, the crack being mostly planar for most of TBC systems analyzed [14]. The second point of the LASAT method applied to TBCs processed by EB-PVD is based on the use of non-destructive techniques (NDT) such as infrared thermography (IRT) and profilometry to characterize debonding and blistering of the debonded area, respectively. The use of IRT consists in heating the substrate at low temperature (50–60 °C) and then measuring the surface temperature of the material, where the lowest temperature corresponds to the debonded area associated with the air gap between the TC and TGO layers [15].

The aim of this paper is to determine by LASAT if CMAS infiltration alters the toughness of the TC layer and if LASAT is able to track the local changes in mechanical properties and localization of weakened zones induced by the corrosive attack.

## 2. Experimental procedure

## 2.1. Specimens and CMAS infiltration

Specimens consist of the superalloy Nimonic 90, machined as buttons (30 mm diameter and 3.29 mm thick). EB-PVD NiCoCrAlY bond coat with a thickness of 100  $\mu m$  was deposited, then a deposit of 210  $\mu m$  thick EB-PVD 7YSZ layer was processed, Fig. 1(a). All coatings were processed by DLR. The samples are detailed in Table 1. The reference sample without prior CMAS infiltration was considered for furnace cycle test (FCT). The FCT corresponds to 50 min dwell time at a temperature of 1100 °C and 10 min cooling time. 30 FCT cycles have been applied to promote a decohesion at the TC/TGO interface when using the LASAT [13].

On a second sample, the CMAS with a nominal composition of  $C_{25}M_{12}A_{11}S_{42}Fe_9Ti_{1.6}$  was deposited as a paste in the amounts of 10 mg/cm² on a circular area of 22 mm in diameter and infiltrated for 1 h under thermal gradient. The procured TBC coated buttons were specially prepared to be tested in a special testing rig which simulates thermal gradient test (TeGra) conditions. This system holds the button in place and heats up the top TBC surface using a  $CH_4+O_2$  burner. Additionally, it provides back side air cooling to the tested specimen as shown in

**Table 1** specimens analyzed in this study for substrate of 30 mm in diameter and 3 mm in thickness.

Sample	Substrate	CMAS	TC thickness	Heat exposure	Analysis
Ref.	Nimonic 90	no	~210 µm	$30 \times 50$ min- cycles (FCT) at 1100 °C and 10 min cooling	Laser shock series with increasing energy
CMAS1	Nimonic 90	Partial in depth and over a 22 mm diameter	~210 µm	single heating – thermal gradient (1250/ 1030 °C) –1 h	Series of LASAT single shock (same energy)

Fig. 1. So a thermal gradient is established within the coating as experienced in a real gas turbine. Additionally, Fig. 1(b) shows the actual TeGra system set up with all its main components (pyrometer, thermocouple, burner and tested specimen). Fig. 1(c) shows an actual CMAS infiltration test in progress where the coated coupon is seen on top with the deposited CMAS layer on its surface.

TBC surface temperature was maintained at 1250 °C  $\pm$  10 °C and the back-side cooling was adjusted to provide a 200 °C gradient over the 2.21 mm distance between the top surface and the thermo couple insert (as shown in Fig. 1(a)). The top surface temperature was monitored using a long wavelength (9–11  $\mu m$ ) pyrometer for which the emissivity radiation was calibrated for the as coated 7YSZ top coat. The isothermal heating was performed for 1 h and the corresponding heating profile of

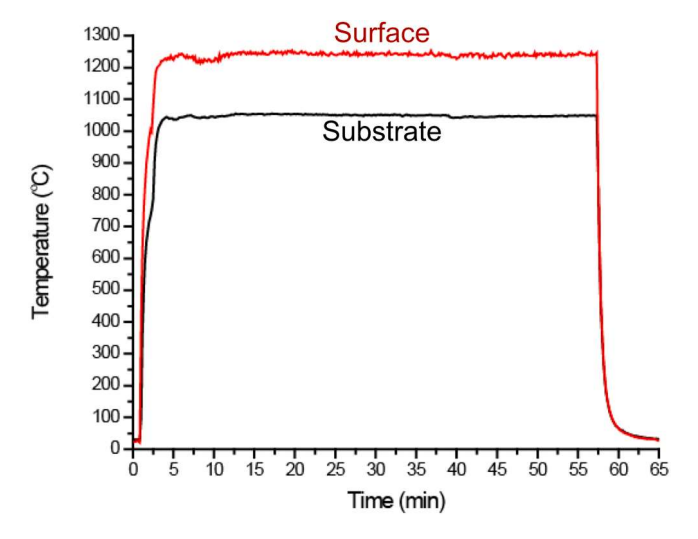


Fig. 2. Isothermal test for CMAS 1 infiltration.

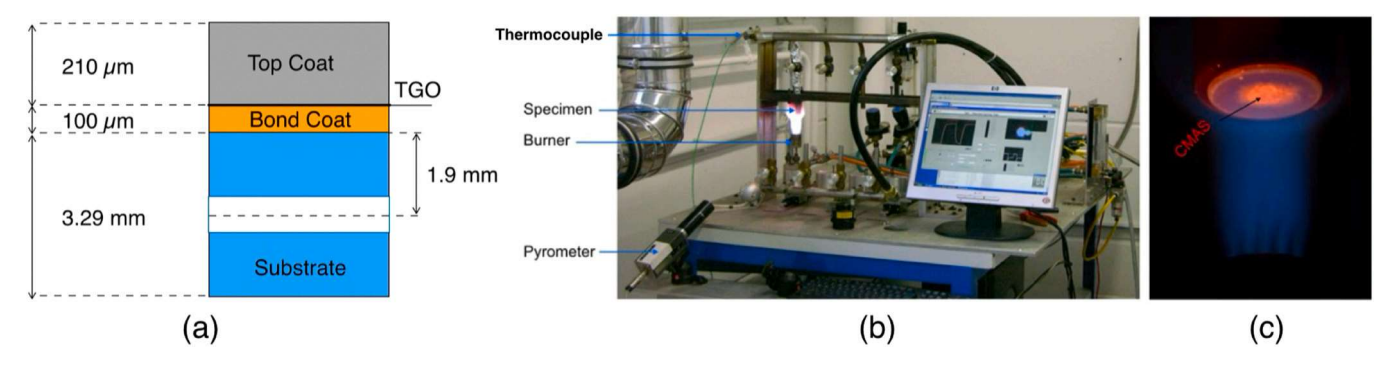


Fig. 1. (a) Specimen dimensions with the location of the thermocouple indicated as a dotted line in the sketched hole in the substrate (b) Tegra system set up with main components indicated (c) Close-up of the running test showing the CMAS deposited layer in the sample and the burner flame.

the conducted experiments is shown in Fig. 2. Additionally, the red line in Fig. 2 shows the TBC surface temperature monitoring from the pyrometer. Whereas the black line represents the substrate temperature (1.9 mm below the BC) monitoring recorded from the inserted thermocouple device. The temperature of the BC can be estimated by using a method described elsewhere [9].

## 2.2. LASAT, infrared thermography (IRT) and profilometer

The LASER used for the LASAT process is a SAGA Thales system, operating on a Nd-YAG source with a wavelength of  $\lambda=532$  nm and a maximum energy of 2 J. A black ablator tape is applied to absorb the laser energy, while a transparent tape is used to confine a small amount of air, facilitating plasma generation. The specific energy levels used for LASAT are described in the following sections.

After laser shock testing, decohesion may be observed as a white spot effect in EB-PVD coatings [13,14]. However, Infrared Thermography (IRT) significantly enhances the measurement of debonding [15–18]. During this process, samples are heated on a plate set to  $50–60~^{\circ}\mathrm{C}$  from the substrate side, while an IR camera monitors the TC side. Debonding is detected as a localized temperature drop, caused by the thermal resistance introduced by TBC delamination and the resulting air gap between the substrate and the ceramic top coat.

To measure the surface roughness of the specimen, after LASAT and/or after CMAS infiltration, a 3D ALTISURF optical profilometer was used. Both mapping and lines can be deduced from these measurements, with a theoretical resolution of 25 nm in depth.

#### 3. Results

## 3.1. Reference sample

The LASAT was first calibrated on the reference material using a laser shock size of 3 mm and increasing laser energy to plot the so-called LASAT curve, establishing the relationship between laser energy and debonded diameter, Fig. 3(a), which corresponds to the infrared thermography (IRT) observations detailed in Fig. 4(a). The reference sample provides a debonding threshold of 1.75 GW/cm², beyond which a progressive increase in debonded area is observed as a function of laser power density, Fig. 3(a).

Meanwhile, for each spot, it is also possible to report the height of blisters  $(\delta)$  induced by each debonding associated with local release of compressive residual stress, Fig. 3(b) and sketch in Fig. 3(c) for a blister diameter (D) and height  $(\delta)$ . The height measurements correspond to roughness observations as shown in Fig. 4(c) and (d) for one blister.

Blistering is also sensitive to the debonded diameter, Fig. 3(b). Below about 0.25 mm diameter, no blistering is observed, while above 0.5 mm diameter, a significant increase in height is observed. It is worth noting

that the height of the blister remains in the same order of magnitude as compared to thinner TBCs previously studied: at 2 mm debonded diameter, the measured height of the blister was of 5  $\mu m$  for a 150  $\mu m$  thick TC [18], and in the present study the blister reaches 6  $\mu m$  for a 210  $\mu m$  thick TC. The difference in TC thickness may have been compensated for the differences in either residual stress or Young's modulus of the TC.

In order to clarify the weakest point of the crack initiation in the tested TBC system, a cross section is performed: Fig. 5(a) and (b) show that after 30 cycles, LASAT promotes a crack mainly located at the TC/ TGO interface, with some residual TGO adhering to the TC, Fig. 5(b). This is in agreement with previous studies based on EB-PVD/(Ni,Pt)Al coatings [13,16]. Incidentally, this result is of great interest for the MCrAlY bond coat, since both the higher roughness and the larger scatter in the TGO thickness compared to the (Ni,Pt)Al bond coat could make the crack more complex. In a similar TBC (EB-PVD MCrAlY), cracks were observed in the lower part of the TBC layer with a complex 3D morphology [17]. In other words, as for the (Ni,Pt)Al/EB-PVD YSZ systems, a few thermal cycles (here limited to 30 FCT) has increased the TC bulk toughness near the interface. In such a condition, the TC/TGO interface becomes the lowest toughness region of the MCrAlY/EB-PVD YSZ system, as revealed by LASAT when implemented in the absence of CMAS.

# 3.2. CMAS sample

After CMAS deposit and before LASAT, IRT diagnosis and surface roughness measurement were performed, Fig. 6(a) and (d). Temperature of the surface is heterogeneous as compared to reference sample, compare Figs. 4(a) to 6(a). In addition to that, the amplitude of the surface roughness is also very high, Fig. 6(d). This temperature heterogeneity can be induced by both thickness variation and conductivity/emissivity modification in the presence of CMAS. In short, this shows that the CMAS deposit is heterogeneous.

Due to this heterogeneity, instead of varying the laser energy, a series of laser shocks at different positions of the sample with a constant given laser energy were applied to the CMAS sample, considering the LASAT characterization. This allows the role of local heterogeneity on the crack characteristics assessed by LASAT to be evaluated by measuring and comparing the crack diameters. Thus, for the CMAS infiltrated sample, the chosen laser energy was set to  $4.3 \pm 0.1~\text{GW/cm}^2$ . This energy corresponds to a debonding and blistering state, for the reference material, that is as easy to measure as possible: the blister height is 4  $\mu$ m and the blister diameter is 1.6 mm, Fig. 3(a) and (b), so that the values are high enough to overcome the measurement uncertainties and low enough to avoid any cracking or spallation of the TC, Fig. 4(a) and (b).

The laser shocks were mostly applied within the CMAS deposit (points 1–6, Fig. 6(b)), with one point tested outside the CMAS deposit,

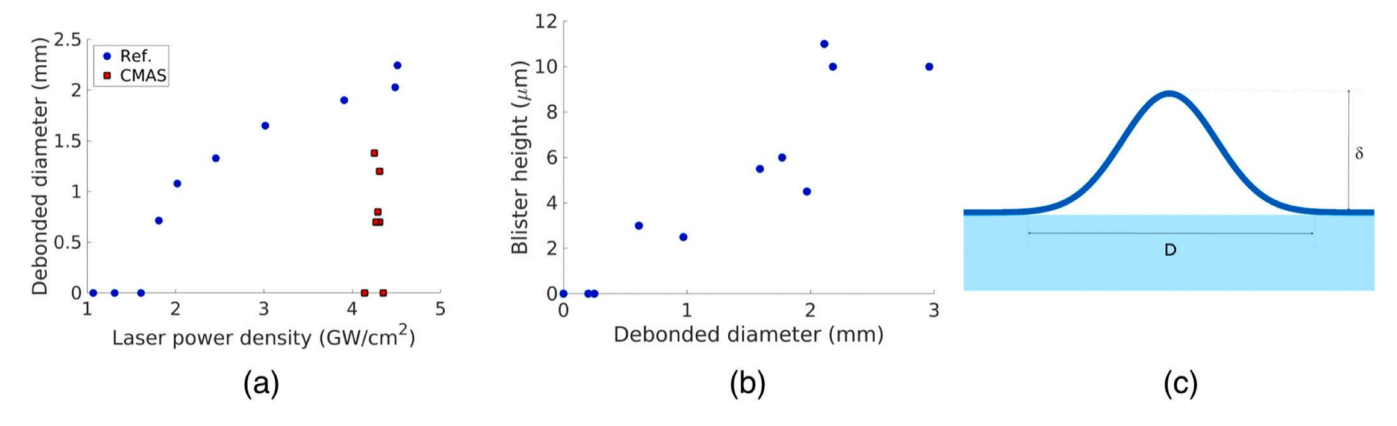


Fig. 3. LASAT test results (a) debonded diameter function of laser power density for reference and CMAS samples (b) blister height function of debonded diameter for reference sample (c) sketch of a typical blister with diameter D and height  $\delta$ .

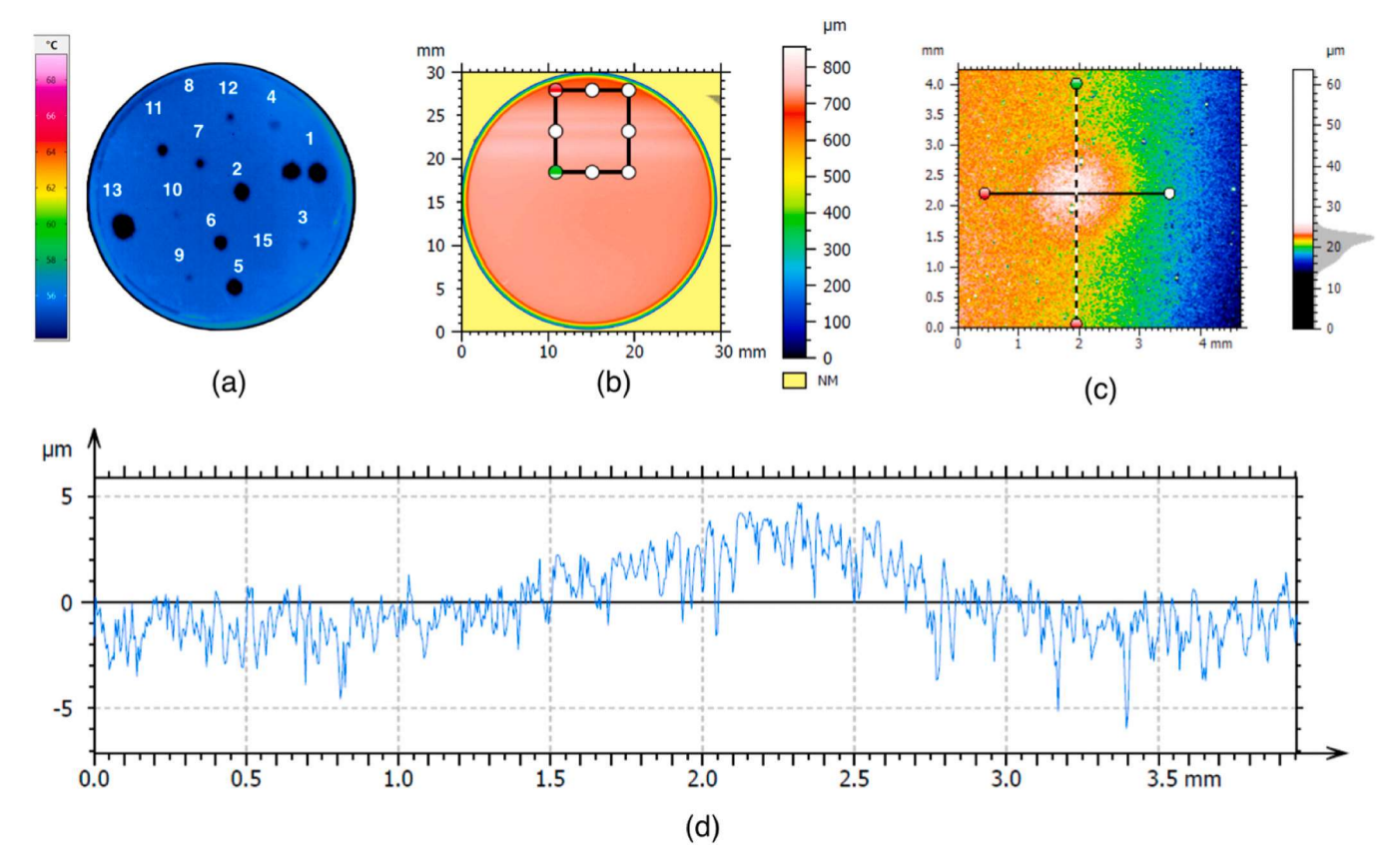


Fig. 4. Reference sample of 30 mm in diameter (a) temperature measurement by IRT after LASAT – the substrate being heated, (b) surface roughness measurement, (c) detail of a blister corresponding to the black square in (b); (d) surface profile along the horizontal line in (c) after correction of the mean slope.

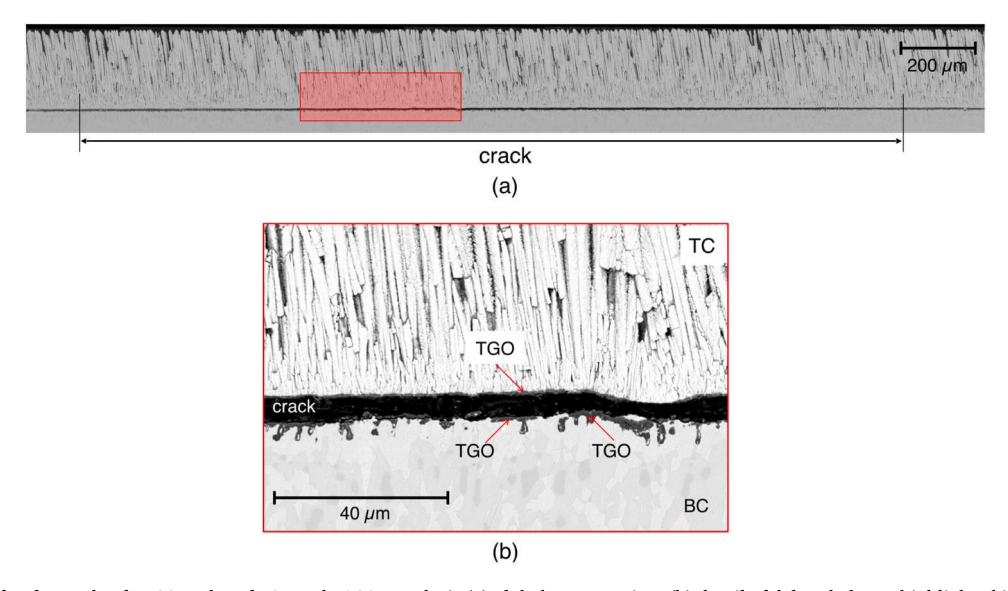


Fig. 5. cross-section of Ref. sample after 30 cycles of FCT and LASAT analysis (a) global cross-section, (b) detail of debonded area highlighted in red in (a), red arrows indicate TGO.

see label 7, Fig. 6(b). The surface imaging of a CMAS infiltrated sample with the IRT camera is more complex than for a sample with a flat topcoat surface: the measurement of the debonded area is indeed a measurement of a global thermal resistance of the TC/air gap (if induced by LASAT)/substrate. However, the heterogeneity of the deposit induces a modification of both the local conductivity and the emissivity, due to both contrast modification and uneven aspects of the surface. The conductivity can be affected by the local infiltration of CMAS and the

thermal resistance by the effective height of the TC plus deposit, Fig. 6 (d). These complex features limit the resolution quality of IRT images, or at least the ease of interpretation of debonding, Fig. 6(b). On the other hand, it is also possible to assume that local temperature variations are still associated with cracking, which should be carefully investigated with cross-sectional analysis.

From IRT measurements, the observed scatter in the debonded diameter in the CMAS sample is very high compared to all known results

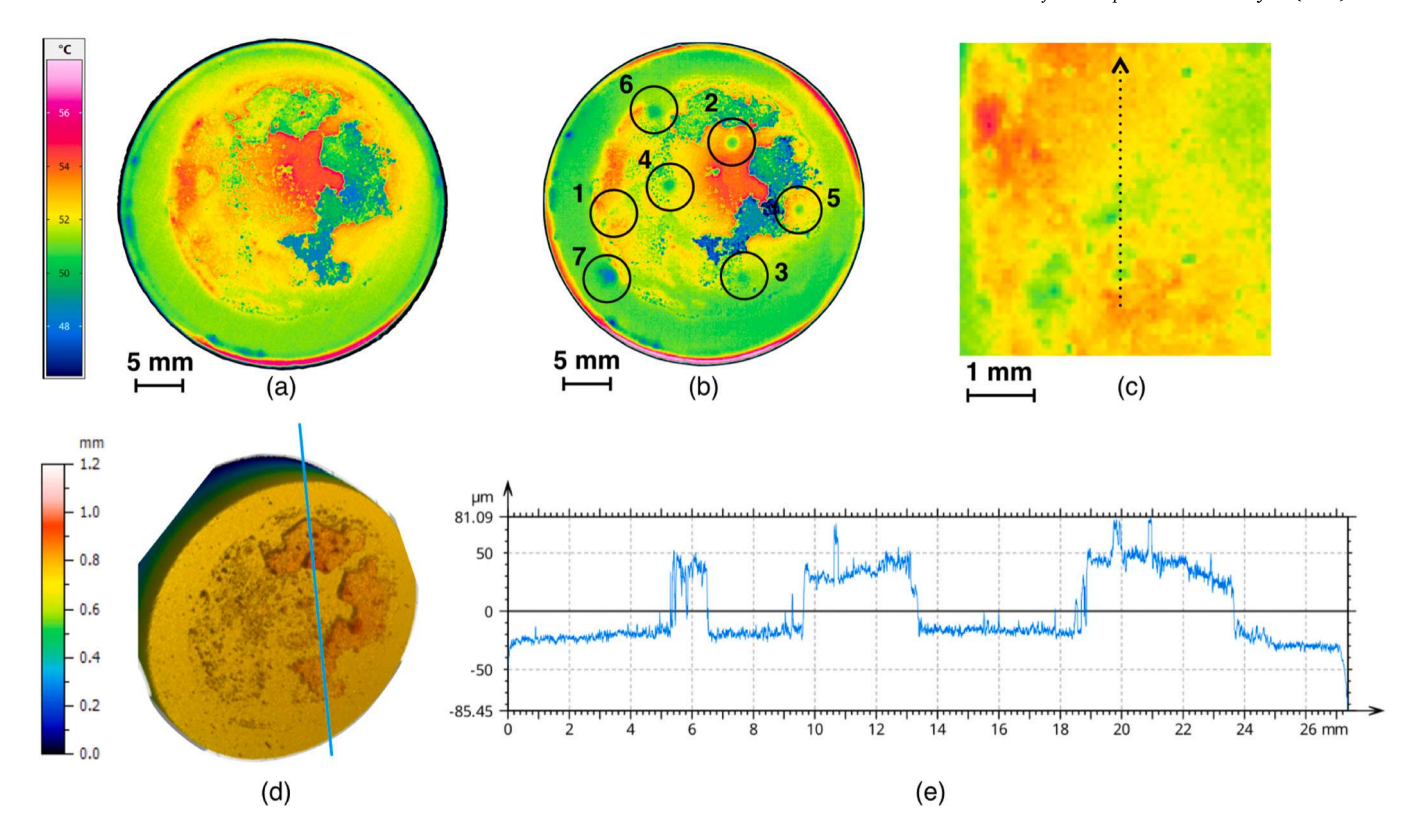


Fig. 6. CMAS sample of 30 mm in diameter (a) temperature measurement by IRT before LASAT (b) temperature measurement by IRT after LASAT, (c) detail of (b) for shock #1 the dashed arrow indicates the cross-sectional area of Fig. 7, (d) surface roughness measurement (e) roughness profile corresponding to the blue line in (d).

in the literature [18–20], as shown in Fig. 3(a). Some laser shocks result in unmeasurable debonding, while others are scattered to values below the observed debonding without CMAS (see Fig. 3(a) and compare Figs. 4(a) and 6(b)). Due to the large additional roughness induced by the CMAS deposit, no clear blistering can be measured for the CMAS sample after LASAT, Fig. 6(d) and (e).

To gain insight into LASAT in the presence of CMAS, a series of cross sections were cut using the reference lines observed in Fig. 6(c) and metallographically prepared for SEM analysis. The focus here is on a cross section corresponding to the direction of the arrow through laser shock #1, Fig. 6(c). Other cross sections give very similar results.

The use of a large cross section allows a clear view of several features specific to LASAT in the presence of CMAS, Fig. 7 (compare with Fig. 5 (a) and (b) for the sample without CMAS). Global points arising from this observation are a large number of cracks at different locations within the height of the TC layer, traces of CMAS residue on the top surface, and a very uniform TGO layer along the entire cross section. The cracks fall into three categories: First, the largest cracks were initiated at the TGO interface, see labels  $A_1$  to  $A_4$  in Fig. 7. Second, at positions  $B_1$  to  $B_4$  in Fig. 7, these cracks clearly grow into the TC layer, forming

branched cracks in the dense, lower part of the TC. Finally, smaller cracks are observed near the top of the TC layer, see labels  $C_1$  and  $C_2$  in Fig. 7.

From a mechanical point of view, these observations highlight that the vicinity of the TGO layer remains a low toughness region, as observed without CMAS. Most importantly, the crack branches indicate a large change in toughness in the TC layer, which has never been observed in EB-PVD YSZ. This proves for the first time that LASAT detects embrittlement of the TC by CMAS infiltration. Smaller cracks located in the upper part of the TC layer also demonstrate an unseen behavior of EB-PVD YSZ, again CMAS infiltration allows crack initiation within the affected areas.

EDS elemental mapping of Si was also performed on laser shock #1 to determine the depth of CMAS infiltration (with Si being the major CMAS component). Fig. 8 shows that molten CMAS has partially infiltrated the TC without reaching the TGO. The infiltrated TC areas can be distinguished by the amount of CMAS locally detected by EDS: While many areas show moderate infiltration of the smaller intercolumnar gaps, selected sections contain significantly more CMAS in larger pockets and a greater amount of CMAS residue remains on top of the TC.

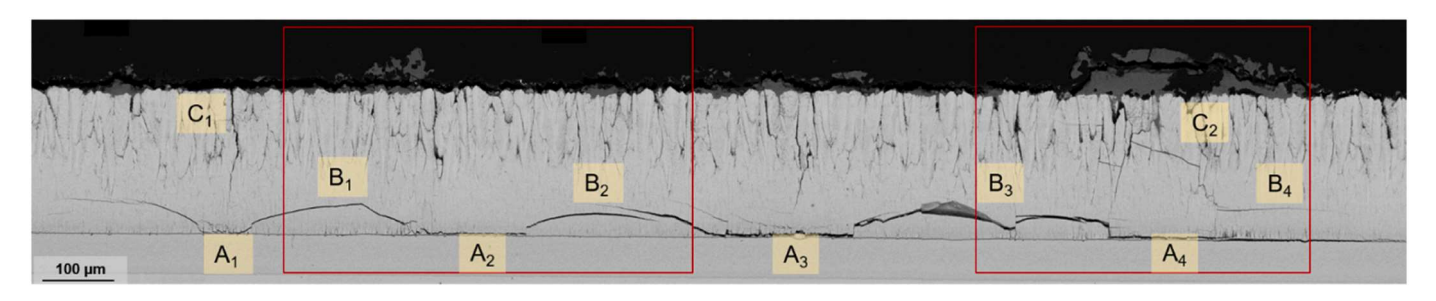


Fig. 7. cross-section of CMAS infiltrated TBC sample after LASAT corresponding to shock #1 in Fig. 6(c); A<sub>i</sub>: cracks at TGO, B<sub>i</sub>: branched crack slighted above TGO, C<sub>i</sub>: crack networks. Red rectangles: extracts of additional SEM-EDS examination, see Fig. 8.

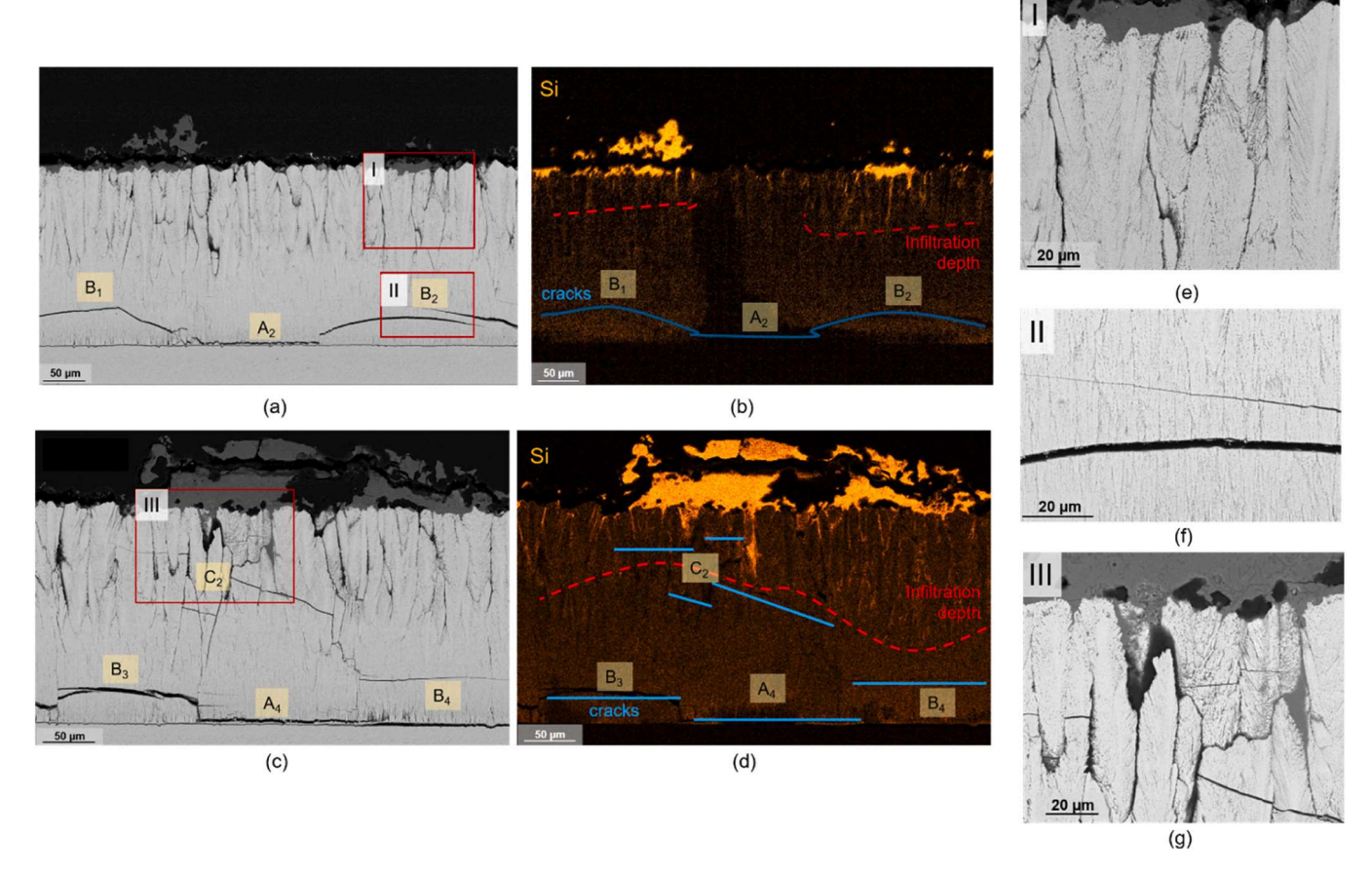


Fig. 8. (a) and (c): SEM extracts corresponding to red rectangles in Fig. 7, (b) and (d): their respective EDS maps of Si signals, and (e) to (g): details of TC affected differently by CMAS: (e) TC above branched crack B<sub>2</sub>; (f) dense TC at branched crack B<sub>2</sub>; (g) TC at crack network C<sub>2</sub>.

Some areas showed only a few microns of infiltration.

By overlaying the crack locations and the infiltration profile, a correlation between the two sets can be assumed: In areas with little or no CMAS infiltration, the cracks are observed close to the TGO (A1, A2 and A3, Figs. 7 and 8). The branching of the cracks from the TGO towards the lower part of the TC layer (B1 and B2) occurred systematically below a detectable CMAS infiltration in the upper part in this current studied sample. Finally, a network of smaller cracks formed in the upper part of the TC layer where the most intense infiltration occurred (see C2 in Fig. 7 and Fig. 8(d)). Below these networks, several cracks are also observed in the lower part of the TC layer, see label A4 below C2 in Figs. 7 and 8.

# 4. Discussion

#### 4.1. Comparison with state-of-the art

This study presents an in-depth analysis of LASAT for an EB-PVD TBC system, which differs from the standard used in previous studies in two main aspects: most of the recent LASAT results have been obtained for a TBC system implying a diffusion bond coat of (Ni,Pt)Al [13–16,18,20], whereas here it is an overlay MCrAlY bond coat. In addition, the thickness of the top coat layer was in the range of 120–150  $\mu m$ , whereas here it is more than 200  $\mu m$ . As a first important result of the present study, LASAT on the tested system in the as-received state yields to the same debonding location, as observed in previous studies: cracks induced by LASAT are close to the TGO/TC interface.

Exposure of a TBC to molten CMAS leads to infiltration of the columnar structure of the tested EB-PVD top coat. Due to variation of the temperature of the flame over the surface the infiltration is often heterogeneous. Both the (heterogeneous) penetration of CMAS and the

surface deposit, which induces local height modification, affect the shock wave propagation as it will be detailed in the next section. For the first time, LASAT induced cracks are observed in the presence of CMAS and their location and morphology vary strongly with respect to those in non-infiltrated samples.

In the presence of CMAS, three variants of cracks are observed in SEM cross-sections: close to the TGO/TC interface (A-cracks in Figs. 7 and 8), within the topcoat layer out of the CMAS infiltrated area (B-cracks in Figs. 7 and 8), and within the CMAS infiltrated area or in the vicinity of infiltrated/non-infiltrated areas (C-cracks in Figs. 7 and 8).

Without CMAS, the morphology of LASAT cracks is associated with a planar disk orthogonal to the direction of the shock wave (for the condition of thickness to diameter of the pulse as used in the present study). With CMAS, the morphology of the cracks is much more complex, it could be associated with small cracks, as observed for C-cracks in Figs. 7 and 8, with a shape not orthogonal to the main shock wave direction. This suggests that locally the infiltrated area, and its potential effect on local toughness, is not homogeneous, yielding to an interface between infiltrated and non-infiltrated area that is not orthogonal to the columns. On the other hand, the branches of B-cracks in Figs. 7 and 8 may be the result of a complex densification/toughness reduction path but could be either the result of crack propagation and deviation from A-cracks or "independent" cracks resulting from the shock wave propagation. The associated morphology of B-cracks, when resulting from A-crack propagation, may be "curved disks" or partial cracks. This requires 3D measurements by either focused ion beam (FIB) or X-ray computed tomography (X-CT) to clarify [17,21].

# 4.2. Potential scenarios of shock wave propagation and cracking mechanisms

The path of a LASAT shock wave can be assumed to be mostly parallel to the interfaces of the TBC, see green bar and arrows in Fig. 9. It has been observed from finite element analysis that lateral effect of shock wave propagation can induce larger crack than the laser shock spot diameter, which is defined as 2D propagation. In addition to that, multiple reflections/diffractions can occur when the shock wave crosses defects: micro-cracks, voids and interfaces [20,22–24]. It is worth noting that the columnar structure of the EB-PVD topcoat could also play a key role in shock wave propagation: if deflection of the shock wave occurs at interfaces, the column itself could guide the wave, resulting in a "1D" propagation mode: the shock wave propagates in both compression (forward) and tension (backward) along the column itself with no or low

energy loss associated with lateral propagation (the analogy could be made with an optical fiber guiding light "1D" propagation, as compared to a source of light emitting in all spaces directions "2D" propagation). Nevertheless, for most of the TBCs studied (APS or EB-PVD), the assumption of a homogeneous shock wave is consistent with both experimental observations (high speed velocity measurements at the free surface) and numerical modeling through finite element analysis of shock wave propagation [14,20,22,23]. The main point of the shock wave propagation in LASAT is that it is mainly compressive on the first path (from the substrate to the free surface of the topcoat, Fig. 9, 2nd row) and becomes mainly tensile after the first reflection at the free surface of the topcoat (Fig. 9, 3rd & 4th row). Multiple reflections occur, but are of lower energy, inducing lower stress value to initiate crack: in a nutshell, after the first reflection, if the tensile stress level is above the strength of the material, a crack will be initiated, if not, no crack will

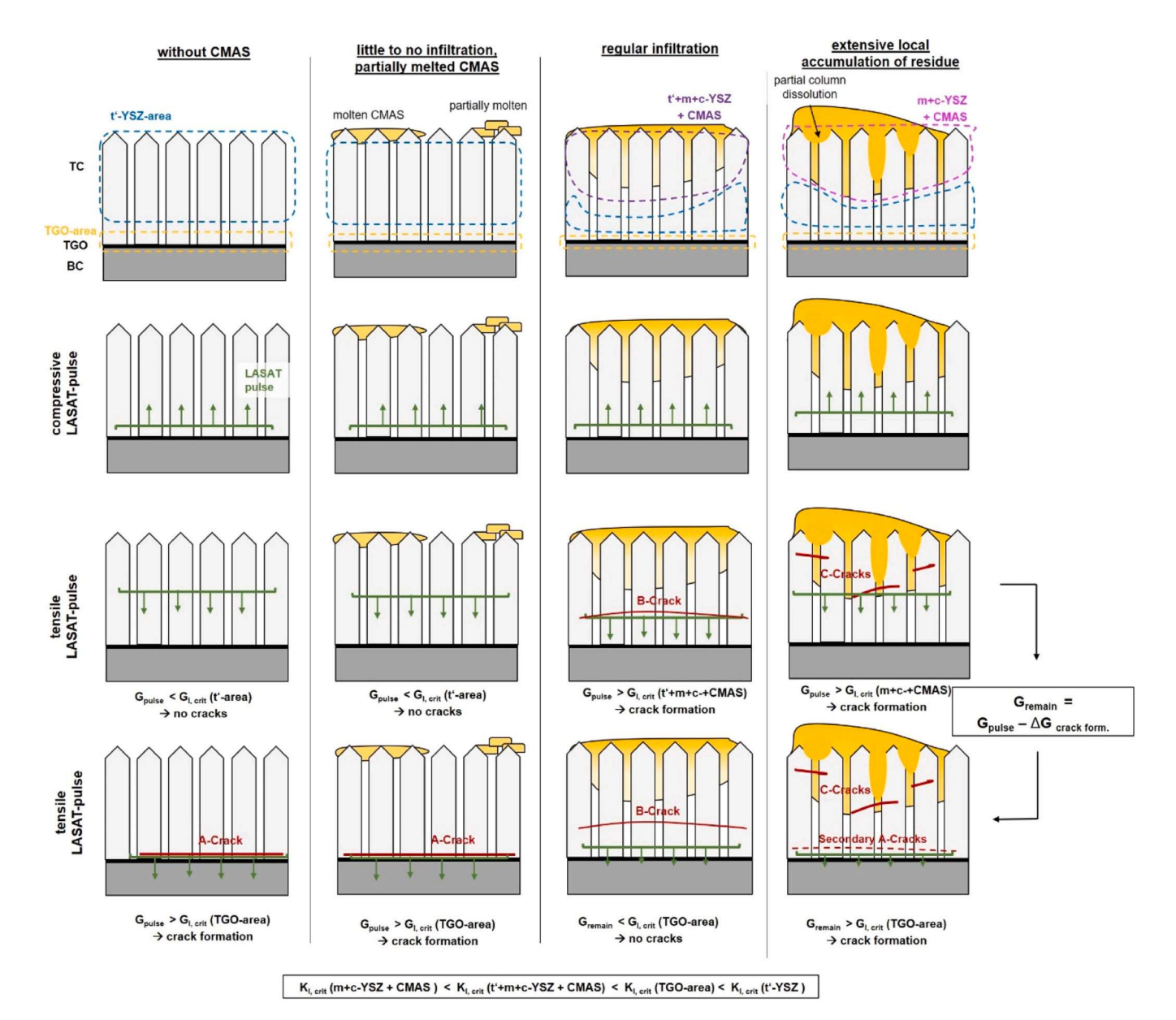


Fig. 9. Schematic LASAT shock wave propagation and crack formation in EB-PVD TBCs for different exemplary cases of CMAS exposure and infiltration: 1st column: without CMAS, 2nd col.: little to no infiltration, partially molten CMAS, 3rd col.: regular infiltration, 4th col: extensive accumulation of CMAS residue. Dashed lines in 1st row: areas with similar phase composition and toughness. G is related to the energy, associated with the laser pulse and induced shock wave probation  $G_{pulse}$ , and to the energy available/remaining after crack formation  $G_{remain}$ . The toughness can be described either by the associated critical energy  $G_{I,crit}$ , or the associated critical stress intensity factor in mode I,  $K_{I,crit}$ . Yellow area: CMAS residue in gaps and on top of TC; Green lines: LASAT shock wave; red lines: resulting cracks; light gray: EB-PVD TC columns; black: TGO; dark gray: BC.

occur due to the specific LASAT pulse.

Due to the heterogeneity of both the flame temperature and the CMAS infiltration depth, the LASAT pulse creates a complex failure mode associated with different types of cracks depending on the extent of CMAS attack and infiltration depth, see Fig. 7 and 8. To explain the observed cracks, the crack formation can be divided into several exemplary cases. The complex failure mode is then a superposition of locally different scenarios. Fig. 9 shows a schematic representation of the cracking mechanisms in four cases: absence of CMAS (1st column), little to no infiltration with partial melting (2nd column), regular melting and infiltration (3rd column), and extensive CMAS accumulation and reaction (4th column). Due to the presence of different amounts and locations of CMAS, different phases such as tetragonal prime t', cubic c or monoclinic m-YSZ phases are found throughout the coating. As a result, regions of different phase composition and toughness, K<sub>L</sub> crit(or of different critical energy at failure G<sub>I,crit</sub>) can be expected. If the free energy of the LASAT pulse G<sub>pulse</sub> is greater than the critical energy of the area, through which it passes, cracking will occur. Crack formation partially releases the energy of the shock wave. If the energy is less than the critical energy, no cracks are formed.

For most non-infiltrated EB-PVD coatings, the crack induced by LASAT is located at the TGO/TC interface or at the very bottom of the TC layer [19]. This is related to the first scenario "without CMAS" in the first column of Fig. 9: an A-type crack can be observed when the energy associated with the shock wave reaches the toughness of the material near the interface with the TGO layer. Furthermore, the size of the crack is related to the size of the laser pulse, with the exact size of the crack being determined by both the interfacial toughness and the intensity of the shock wave [14,20]. For simplicity, the crack for non-infiltrated TBC is shown as a TGO/TC interface crack sized to the shock wave path, Fig. 9, first row.

The second scenario "little to no infiltration" (Fig. 9, 2nd column) is observed when the infiltration of CMAS is rather limited to a few microns depth into the TC. It can be assumed that the shock wave through the CMAS infiltrated TBC is homogeneous and that the toughness of the TBC is not modified by the CMAS deposit. Thus, LASAT would produce an A-crack similar to the CMAS-free scenario. Therefore, the very localized effect of CMAS on the top surface of the TBC does not affect the behavior of the TBC.

The third scenario is associated with a "regular infiltration" (Fig. 9 3rd column). In this case, the stiffness of the TC layer is increased and small fractions of the t'-YSZ columns were transformed to monoclinic mand/or cubic c-7YSZ phase. A key point to consider is that the local stress associated with the shock wave, is increased locally as a function of the shock impedance of the material: the higher the stiffness, the higher the shock wave velocity and subsequent stress. Thus, when A- and B-cracks are observed in the presence of CMAS infiltration, this should be the consequence of a limited effect of the infiltration for A-cracks, whereas B-cracks can be the result of both infiltration and corrosive attack of the CMAS and increase of local stress level associated with denser material. Besides, in the area of infiltration the potential effect of the columnar structure could be limited, the shock wave propagation being modified, by the way the "guide" for wave propagation could be lost. That is, the cracks branching out of the CMAS infiltrated zone in the dense part of the TC may have been the result of a strong densification of the TC and subsequent modification of the shock wave behavior. By modifying the stiffness, the toughness of the top layer may also have been modified.

The last scenario is associated with a "maximum corrosive attack", which is observed to correlate more or less with an extensive local accumulation of residues, last column in Fig. 9. In this case, either larger gaps and pockets exist prior to CMAS exposure and are then filled with CMAS, or a stronger reaction of the molten CMAS degrades and dissolves larger portions of the columns. In this case, cracks could be located within the CMAS infiltrated area, C-cracks in Figs. 8 and 9. Again, due to the densification of the material by the infiltration, it is assumed that the stress level increases locally along with a decrease in toughness due to

the corrosive attack by the greater amount of CMAS deposit locally present. This point is fully consistent with the observation of embrittlement in TBC exposed to CMAS and further subjected to furnace cycling, resulting in cracking and spallation associated with the top surface of the TC where corrosive attack is maximized [25]. It is also observed that A- and C-cracks can be associated to the same lateral location. This suggests that after the energy is released by the formation of C-cracks, the shock wave still has enough energy to initiate the formation of additional "secondary" A-cracks at the TC/TGO interface.

# 4.3. Synthesis of the impact of CMAS on phases and mechanical properties as revealed by LASAT

The observed correlation between local CMAS infiltration and crack locations and paths demonstrates that LASAT can identify the weakest points in terms of mechanical strength or toughness in a given topcoat. In the local absence of CMAS for the reference sample, or with little to no infiltration, the weakest location is identified as the TC/TGO interface or locally in the TGO. For drastic effects of CMAS infiltration, cracking is different in the way new crack locations are detected.

In areas of extensive CMAS infiltration with larger filled pockets (Fig. 8(a)), phase transformation from t'-YSZ to m- and c-ZrO2 is likely to occur, see Fig. 8(g) [5,26]. This transformation is more pronounced than in areas of moderate infiltration, Fig. 8(e), or the dense lower TC, Fig. 8 (f). Since both monoclinic and cubic phases as well as CMAS itself are significantly less tough ( $K_{IC}(m)=2-2.6~MPa-m^{1/2}$ ,  $K_{IC}(c)=1-2~MPa-m^{1/2}$  [27],  $K_{IC}(CMAS)=0.6-2~MPa-m^{1/2}$  [28,29]) than the tetragonal prime phase  $(K_{IC}(t')=3 \text{ MPa-m}^{1/2})$ , only a small fraction of the shock wave energy was sufficient to form the microcracks mentioned above. Thus, additional energy remains in the shock wave to form additional cracks near the TGO. This shows that the crack branches follow a path of embrittlement associated with a decrease in local toughness when CMAS infiltration is effective [30,31]. For the TeGra setup tested, densification of the TC layer by sintering is a priori not observed for the EB-PVD system, considering the limited time of exposure to high temperature. Thus, B- and C-cracks are the result of CMAS infiltration, taking into account the associated densification effect. Sintering has been observed with long term exposure to similar gradients in burner rig cycling experiments, but they show only TC/TGO crack localization in the presence of sintering, i.e., despite the increase in Young's modulus due to sintering, only A-cracks are observed [16].

Finally, it should be noted that the above scenarios of local changes in toughness associated with the interface between infiltrated and noninfiltrated regions could be established by the following assumption: both the front shock wave in compression and the back shock wave in tension are a priori uniform. This is consistent with the existing model of shock wave propagation made for homogeneous TBC systems in LASAT mode. Some local effect of shock wave transmission modification could be induced by the local stiffness modification associated with CMAS infiltration, where a priori CMAS could increase the stiffness and associated shock impedance of the system, and ultimately yields higher local stress values. Since the uniaxial aspect of shock wave propagation is the main stress induced by LASAT, the LASAT has revealed the local effect of embrittlement by CMAS infiltration: When cracks are observed in areas never observed to be prone to cracking for EB-PVD YSZ for both cracks parallel to the TGO interface, mainly near the top of the system, and cracks branching to the weakest areas of the YSZ, despite no evidence of infiltration at these points.

#### 5. Conclusions

This study shows that CMAS infiltration controls the local toughness of the top layer of a typical TBC processed by EB-PVD. LASAT was used to clarify where the weakest point of the CMAS infiltrated TBC was located. While in a reference sample the TGO was observed to drive cracking, in the presence of CMAS both the TGO and the "bulk" topcoat

were subject to cracking. To clarify these points, cracks were classified as A-cracks close to the TGO interface, B-cracks within the top coat underneath the infiltrated areas, and C-cracks within the heavily infiltrated areas. Infrared thermography was also found to be relevant for measuring decohesion even in the presence of heterogeneous and complex CMAS deposits. However, the issue of crack localization in the coating thickness could not be directly resolved by simple infrared thermography and requires careful complementary cross sections for further SEM analysis.

In conclusion, the local toughness reduction induced by CMAS infiltration in EB-PVD 7YSZ top coats has been revealed for the first time using the LASAT facility. The above results pave the way for measuring the localization of weak points in the presence of complex deposits such as CMAS, corrosion attack or erosion of TBC systems using the LASAT technique. This could, to some extent, help in the design of optimal CMAS resistant coatings, taking into account their local mechanical properties. To quantify the local toughness value in the presence of CMAS, an in-depth analysis of the shock wave propagation in the presence of densified material is required. Simultaneously, some thermal cycling experiments related to the processing of artificial flaws processed by LASAT in CMAS attacked specimens are underway and will be detailed in a future paper.

#### CRediT authorship contribution statement

Billard Capucine: Writing – review & editing, Software, Methodology, Investigation, Formal analysis, Data curation. Mikulla Christoph: Writing – review & editing, Visualization, Methodology, Investigation, Formal analysis, Data curation. Guipont Vincent: Validation, Supervision, Project administration, Methodology. Naraparaju Ravisankar: Writing – review & editing, Validation, Supervision, Resources, Project administration, Methodology, Funding acquisition, Data curation, Conceptualization. Schulz Uwe: Writing – review & editing, Resources. Maurel Vincent: Writing – review & editing, Writing – original draft, Validation, Supervision, Project administration, Methodology, Funding acquisition, Formal analysis, Data curation, Conceptualization.

#### **Declaration of Competing Interest**

The authors declare that they have no known competing financial interests or personal relationships that could have appeared to influence the work reported in this paper.

#### References

- [1] D.A. Shifler, S.R. Choi, in: "CMAS effects on ship gas-turbine components/ materials." Turbo Expo: Power for Land, Sea and Air 50985, American Society of Mechanical Engineers, 2018.
- [2] M.H. Vidal-Setif, et al., "Calcium-magnesium-alumino-silicate (CMAS) degradation of EB-PVD thermal barrier coatings: characterization of CMAS damage on ex-service high pressure blade TBCs, Surf. Coat. Technol. 208 (2012) 39–45.
- [3] R. Naraparaju, et al., Degradation study of 7wt% yttria stabilised zirconia (7YSZ) thermal barrier coatings on aero-engine combustion chamber parts due to infiltration by different CaO-MgO-Al2O3-SiO2 variants, Surf. Coat. Technol. 260 (2014) 73-81.
- [4] R. Naraparaju, M. Huttermann, U. Schulz, P. Mechnich, Tailoring the EB-PVD columnar microstructure to mitigate the infiltration of CMAS in 7YSZ thermal barrier coatings, J. Eur. Ceram. Soc. 37 (1) (2017) 261–270.
- [5] Z. Stein, et al., Residual stress effects of CMAS infiltration in high temperature jet engine ceramic coatings captured non-destructively with confocal Raman-based 3D rendering, J. Eur. Ceram. Soc. 43 (4) (2023) 1579–1589.

- [6] C. Mercer, et al., "A delamination mechanism for thermal barrier coatings subject to calcium-magnesium-alumino-silicate (CMAS) infiltration, Acta Mater. 53 (4) (2005) 1029–1039.
- [7] Jing Wu, et al., "Microstructure and thermo-physical properties of yttria stabilized zirconia coatings with CMAS deposits, J. Eur. Ceram. Soc. 31 (10) (2011) 1881–1888.
- [8] David L. Poerschke, Carlos G. Levi, "Effects of cation substitution and temperature on the interaction between thermal barrier oxides and molten CMAS, J. Eur. Ceram. Soc. 35 (2) (2015) 681–691.
- [9] R. Naraparaju, et al., Integrated testing approach using a customized micro turbine for a volcanic ash and CMAS related degradation study of thermal barrier coatings, Surf. Coat. Technol. 337 (2018) 198–208.
- [10] J.J. Gomez Chavez, et al., Effects of yttria content on the CMAS infiltration resistance of yttria stabilized thermal barrier coatings system, J. Mater. Sci. Technol. (2019).
- [11] J.J. Gomez Chavez, et al., Comparative study of EB-PVD gadolinium-zirconate and yttria-rich zirconia coatings performance against Fe-containing calciummagnesium-aluminosilicate (CMAS) infiltration, Corros. Sci. (2021) 109660.
- [12] C. Mikulla, et al., Microstructure refinement of EB-PVD gadolinium zirconate thermal barrier coatings to improve their CMAS resistance, Coatings 13 (5) (2023).
- [13] Vincent Guipont, et al., "Buckling and interface strength analyses of thermal barrier coatings combining laser shock adhesion test to thermal cycling, Surf. Coat. Technol. 378 (2019) 124938.
- [14] Fabre, Grégory, et al., "Laser shock adhesion test (LASAT) of electron beam physical vapor deposited thermal barrier coatings (EB-PVD TBCs), Adv. Mater. Res. 278 (2011) 509–514.
- [15] Vincent Maurel, et al., "Thermal cycling damage monitoring of thermal barrier coating assisted with LASAT (LAser Shock Adhesion Test), Surf. Coat. Technol. 380 (2019) 125048.
- [16] Lara Mahfouz, et al., "Thermal barrier coatings in burner rig experiment analyzed through laser shock for damage monitoring (LASDAM) method, J. Eur. Ceram. Soc. (2024).
- [17] Anne Dennstedt, et al., "Three-dimensional characterization of cracks in a columnar thermal barrier coating system for gas turbine applications, Integr. Mater. Manuf. Innov. 8 (2019) 400–412.
- [18] L. Mahfouz, B. Marchand, V. Guipont, F. Coudon, V. Maurel, Driving forces in thermal barrier coatings blistering, Materialia 28 (2023) 101728.
- [19] Vincent Guipont, et al., "Bond strength determination of hydroxyapatite coatings on Ti-6Al-4V substrates using the laser shock adhesion test (LASAT), J. Biomed. Mater. Res. Part A 95 (4) (2010) 1096–1104.
- [20] G. Bégué, G. Fabre, V. Guipont, M. Jeandin, P. Bilhe, J.Y. Guedou, F. Lepoutre, Laser shock adhesion test (LASAT) of EB-PVD TBCs: towards an industrial application, Surf. Coat. Technol. 237 (2013) 305–312.
- [21] V. Maurel, L. Helfen, R. Soulignac, T.F. Morgeneyer, A. Koster, L. Rémy, Three-dimensional damage evolution measurement in EB-PVD TBCs using synchrotron laminography, Oxid. Met. 79 (2013) 313–323.
- [22] Cuq-Lelandais J.P. Etude du comportement dynamique de matériaux sous choc laser subpicoseconde (Doctoral dissertation in French, ISAE-ENSMA Ecole Nationale Supérieure de Mécanique et d'Aérotechique-Poitiers).
- [23] M. Arrigoni, J.P. Cuq-Lelandais, M. Boustie, E. Gay, L. Berthe, An industrial challenge based on the wave propagation: the shock adhesion test. Wave Propagation, AcademyPublish Ed, WY (USA), 2012.
- [24] L. Berthe, M. Arrigoni, M. Boustie, J.P. Cuq-Lelandais, C. Broussillou, G. Fabre, M. Jeandin, V. Guipont, M. Nivard, State-of-the-art laser adhesion test (LASAT), Nondestruct. Test. Eval. 26 (3-4) (2011) 303–317.
- [25] H. Peng, L. Wang, L. Guo, W. Miao, H. Guo, S. Gong, Degradation of EB-PVD thermal barrier coatings caused by CMAS deposits, Prog. Nat. Sci.: Mater. Int. 22 (5) (2012) 461–467.
- [26] L. Steinberg, R. Naraparaju, M. Heckert, C. Mikulla, U. Schulz, C. Leyens, Erosion behavior of EB-PVD 7YSZ coatings under corrosion/erosion regime: effect of TBC microstructure and the CMAS chemistry, J. Eur. Ceram. Soc. 38 (15) (2018) 5101–5112.
- [27] C. Mercer, J.R. Williams, D.R. Clarke, A.G. Evans, On a ferroelastic mechanism governing the toughness of metastable tetragonal-prime (t') yttria-stabilized zirconia, Proc. R. Soc. A: Math., Phys. Eng. Sci. 463 (2081) (2007) 1393–1408.
- [28] V.L. Wiesner, N.P. Bansal, Mechanical and thermal properties of calcium-magnesium aluminosilicate (CMAS) glass, J. Eur. Ceram. Soc. 35 (10) (2015) 2907–2914.
- [29] G. Bolelli, et al., BAS, CMAS and CZAS glass coatings deposited by plasma spraying, J. Eur. Ceram. Soc. 27 (16) (2007) 4575–4588.
- [30] Y. Sun, X. Nie, C. Cai, et al., Phase transformation failure in YSZ TBCs induced by component-dependent CMAS corrosion, Surf. Coat. Technol. 464 (2023) 129547.
- [31] Q. Zhou, Y. Wei, G. Xu, et al., Microstructure and microcrack evolution mechanism of thermal barrier coatings under CMAS infiltration and corrosion: experimental and numerical modeling, Corros. Sci. 229 (2024) 111890.